

# Design and Validation of Scalable Reconfigurable Intelligent Surfaces

Marco Rossanese<sup>a,\*</sup>, Placido Mursia<sup>a</sup>, Andres Garcia-Saavedra<sup>a</sup>, Vincenzo Sciancalepore<sup>a</sup>, Arash Asadi<sup>b</sup>, Xavier Costa-Perez<sup>a,c,d</sup>

<sup>a</sup>NEC Laboratories Europe GmbH, Heidelberg, Germany

<sup>b</sup>Technischen Universität Darmstadt, Darmstadt, Germany

<sup>c</sup>i2CAT Foundation, Barcelona, Spain

<sup>d</sup>ICREA, Barcelona, Spain

---

## Abstract

In this paper, we share our experience in designing, prototyping, and empirically characterizing RF Switch-based Reconfigurable Intelligent Surfaces (RIS). Our RIS design consists of arrays of patch antennas, delay lines, and programmable radio-frequency (RF) switches, enabling 3D beamforming passively, *without active RF components*. Our design introduces two key innovations: (i) a modular structure that provides scalability for sustainable deployments, and (ii) the support for 3-bit phase shifters, enabling high-spatial resolution codebooks. We realized this design through PCB technology and affordable electronic components, then rigorously validated our prototype in a controlled setting. With this paper, we make a comprehensive characterization of our RIS publicly available via a large dataset, to promote further empirical-driven research on this topic. Finally, we present a cost analysis of our design, which underscores the importance of sustainable practices in shaping the future of wireless technologies.

**Keywords:** wireless networks, experiments, measurements, characterization

---

## 1. Introduction

The emergence of 6G networks necessitates a fundamental shift in wireless communication systems, emphasizing not only elevated data rates and minimal latency but also underscoring the imperative of *sustainability*. Energy efficiency stands out as a critical concern, propelling the investigation of innovative scalable solutions to mitigate environmental impact. In this context, Reconfigurable Intelligent Surfaces (RISs) have gained prominence as a pivotal technology for the next generation of mobile systems [1].

Despite the recent surge in interest, primarily fueled by theoretical models [2] and simulations, empirical studies are limited due to the unavailability of accessible and affordable RIS prototypes [3]. A RIS is essentially a planar structure comprising reflective cells capable of programmatically modifying the electromagnetic response of incident radio-frequency (RF) signals, inducing changes in phase, amplitude, or polarization.

This capability introduces novel opportunities and heralds a shift in the wireless landscape [4]. Traditionally viewed as an optimization constraint in conventional systems, the wireless environment can now be treated as a variable for optimization, giving rise to the concept of the Smart Radio Environment. For instance, when an obstacle obstructs the line-of-sight (LoS) between the transmitter and receiver, strategically deploying a RIS device can address this issue through passive beamforming. This strategic deployment effectively establishes a virtual LoS, ensuring favorable conditions for signal propagation. Such in-

terventions have the potential to significantly boost the energy efficiency of mobile networks by more than 50% [5].

The aforementioned considerations prompt the development of a scalable and sustainable *passive RIS*, designed to meet the following requirements:

- Shall (re-)steer RF signals with minimal power loss;
- Must not utilize active RF components;
- Must minimize the energy required to reconfigure its reflective cells;
- Shall be reconfigurable in real-time;
- Must be amenable to low-cost production at scale.

Based on this, we embarked on an interdisciplinary journey to design, build and characterize scalable and inexpensive RISs suitable for systems research that satisfies the above stringent requirements.

Besides meeting the usual requirements for a RIS, our approach provides additional features compared to previous work. In contrast to diode-based approaches, usually constrained to 1-bit phase shifters, our design has a resolution of 3 bits, enabling *high spatial resolution codebooks*.

Our modular design permits simultaneous coordination of multiple ( $M$ ) boards, and hence it enables truly *scalable and adaptive structures* of  $M \times N_x \times N_y$  surfaces in a flexible manner. Another unique feature of the design is the capability of full absorption of signal energy, which opens several opportunities. For instance, we can effectively switch off reflective components, which lets us *virtually optimize the shape and the size of the RIS* to meet system constraints. *Switching off* a cell in a RIS is non-trivial when a cell is specifically designed to reflect signals passively, without a direct energy feed that could be cut off.

---

\*Corresponding author

Email address: Marco.Rossanese@nec-lab.eu (Marco Rossanese)

Specifically, we show via extensive experiments that our prototype has high configuration speed (less than 35 ms for 100 cells) and low energy consumption (62 mW with the controller in high-performing mode). These values can be further improved by optimizing the controller firmware, e.g., exploiting the sleeping modes of the microcontroller when a re-configuration is not required.

This manuscript is an extended version of a preliminary workshop paper [6]. Specifically, the novel contributions of this paper can be succinctly summarized as follows:

**Modularity.** We go beyond theoretical analysis by rigorously validating the modularity advantage of our RIS design. Given a RIS board with 10x10 antenna elements, we combine two RIS boards to form a 10x20-element structure and four RIS boards to form a 20x20-element structure. This showcases the ability of our approach to provide scalability and modularity.

**Novel Multi-Beam Codebook.** We introduce an approach to generate multi-beam configurations. By enabling the creation of multiple focused beams, our RISs can maximize the utilization of available resources, thereby achieving spatial multiplexing while minimizing wasteful signal leakage. The multi-beamforming capabilities of our RIS are empirically evaluated in terms of beam precision and associated power drop as compared to the single-beam configuration using a 10x20-element structure comprised of two coordinated RIS boards. This assessment demonstrates the efficiency of our hardware design in achieving advanced beamforming while maintaining accurate signal targeting.

**Enhanced Codebook for Near-Field Conditions.** A new model is introduced to generate codebooks that can effectively cope with near-field conditions. Using our modular prototype, we verify the effectiveness of the near-field-based codebook, essential for addressing challenges posed by close-range signal propagation, with a 20x20 antenna-element antenna element comprised of four coordinated RIS boards.

The paper is organized as follows: Section 2 provides an analysis of a few relevant works. Section 3 describes the RIS design, while Section 4 presents the RIS codebook. Section 5 details the empirical characterization setup, and Section 6 outlines the RIS implementation. Finally, Section 7 presents the results.

## 2. Related work

Among existing literature on prior experiences, [7] discloses a 16x16 RIS operating at 28GHz, whereas [8] introduces a 16x10 RIS working at sub-6GHz with an Arduino control unit where only groups of elements can be configured. Both solutions implement a PIN diode-based RIS with a 1-bit resolution phase shift. Additionally, the prototype presented in [9] obtains a 2-bit phase quantization by using 5 PIN diodes per RIS element, whereas in [10] the use of 3 PIN diodes allows for 8 phase states. [11] discloses a 14x14 RIS based on varactor diodes, which allows continuous control of the phase shifts at the cost of a wide range in control voltages, which is generally hard to achieve.

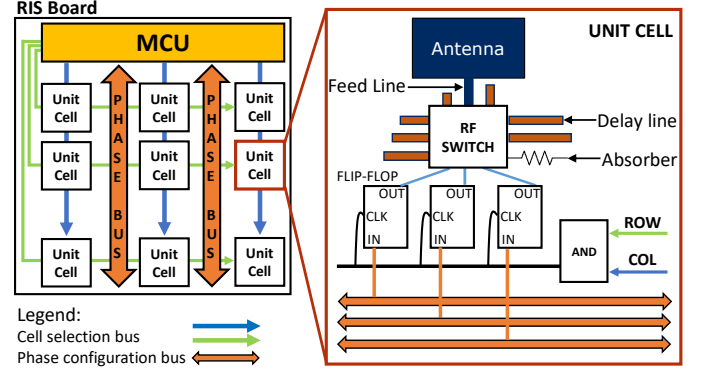


Figure 1: RIS board and unit cell.

Conversely, RF switch-based implementations unveil a lower cost w.r.t. PIN diodes used to control the reflector units. In particular in [12], a RIS prototype with 14x16 reflectors at 60GHz is presented. The unit elements are placed more than one  $\lambda$  away to reduce the mutual coupling at the expense of a tighter maximum scanning angle ( $\lambda$  is the operating wavelength). In [13], 40 reflectors are mounted on the boards, they are  $\lambda/4$  tall,  $\lambda/10$  wide, and separated  $\lambda/10$  on both the x and y-axis. The work shown in [14] allows singular configurations of the elements, thereby reducing the number of utilized pins at controller side. This RIS is made of 4x4 patch antennas operating at 5GHz and controlled with 2-bit phase shifter made with the transmission line method. In [15], the application of a RIS in a vast urban setting and its integration with pre-existing networks is elucidated. Moreover, the radiation pattern of the RIS was formulated utilizing the data from our publicly available dataset, thereby ensuring a high level of authenticity in the simulations.

We showcased the operational capabilities of RIS within a practical indoor setting during a demonstration at ICC Rome 2023. Our presentation effectively illustrated how a transmitting (TX) and a receiving (RX) unit can successfully navigate around an obstacle, thereby overcoming communication disruptions, with the assistance of an RIS. For further details, interested readers can access additional information through the provided link<sup>1</sup>.

## 3. RIS design

The main purpose of our RIS is to perform 3D beamforming passively, i.e., re-focus the energy received from impinging RF signals towards specified directions without active (energy-consuming) RF components. Fig. 1 illustrates a **board** consisting of a grid of  $N_x \times N_y$  **unit cells** distributed in a 2D array. Unit cells are elements that can reflect RF signals with configurable phase shifts.

Phase shifts are configured by a microcontroller unit (MCU), which can be programmed from an external controller. Conventional RIS designs are characterized by dedicated  $N_x \times N_y$  connections from the MCU to each unit cell. However, MCUs only support a limited number of such connections, which constrains

<sup>1</sup>[https://drive.google.com/file/d/1kRKOT2izDz\\_uuVeIHh8m2PFqHwjUfhsZ/view?usp=drive\\_link](https://drive.google.com/file/d/1kRKOT2izDz_uuVeIHh8m2PFqHwjUfhsZ/view?usp=drive_link)

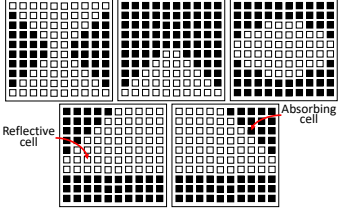


Figure 2: Shape-adaptive RIS.

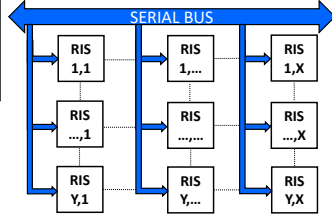


Figure 3: Multi-board RIS.

the maximum number of cells and, consequently, the achievable beamforming gains [16]. A more scalable approach is to connect each cell with a pair of buses, denoted as **column/row cell selection buses**, that *select* the cell to be configured, and a **phase configuration bus**, which communicates the desired configuration index out of a discrete set. In this way, we reduce the complexity of the design from  $N_x \times N_y$  to  $N_x + N_y$  connections per board.

As shown in the right-hand side of Fig. 1, each unit cell connects both column/row selection buses with an **AND** gate. Hence, when the MCU sets a high voltage state in row  $x$  and column  $y$ , the MCU activates the configuration bus for unit cell  $(x, y)$ , whereas all the remaining gates across the board will output a low voltage state (0 V). Each cell also integrates a set of **flip-flop D**, which exploit the high-state exiting the AND gate as a rising edge to update and send out the value stored in memory. We designed our RIS with 3-bit phase shifters, which enable high spatial resolution codebooks. Therefore, each cell uses *three* 1-bit phase configuration buses and *three* flip-flops.

The latter are connected to the **configuration ports** in an **RF switch**. An RF switch is a component that can redirect the RF signal received from an **input port** towards one **output port**, as indicated by the configuration ports. The input port is connected to a **patch antenna**, the ultimate responsible for interacting with the medium, through a **feeding line**. Each output port (except one) uses an open-ended **delay line** with a suitably-designed length to reflect impinging signals with a specific time delay, shifting the signal phase.

We reserve one output port of the RF switch to connect an **absorber**, an impedance-matching component that absorbs the energy of incoming signals instead of reflecting them back. We call this configuration *absorption state*, and it let us virtually optimize the reflective area of the RIS to meet system constraints. For instance, we can flexibly adapt to different time constraints when optimizing the RIS configuration, which takes longer the larger the number of active cells in the RIS. This is illustrated in Fig. 2. Alternatively, an energy harvester [17] may be employed instead to re-use the dissipated energy to feed a low-consuming MCU, becoming self-sustainable boards, which we leave for future work.

Our RIS design is modular: as shown in Fig. 3, multiple boards can be coordinated through a common bus. The disposition of the unit cells across different boards has been carefully designed to have a separation of  $\lambda/2$ , where  $\lambda$  is the operating wavelength. This modular design allows increasing/decreasing the physical area of the RIS structure without compromising the inter-cell distance, as depicted in Fig. 2.

## 4. Beamforming codebook

In this section, we detail the proposed procedure to construct RIS beamforming codebooks under three different settings. Firstly, in the case of single-user transmission, we distinguish between (i) far-field, and (ii) near-field channel propagation conditions between the RIS and both the transmitter and the user. Moreover, we discuss the case of (iii) multi-user transmission (valid for both near and far-field conditions).

### 4.1. Far-field codebook

A RIS board can be modeled as a uniform planar array (UPA) comprised of  $N = N_x \times N_y$  antenna elements [18, 16]. Hence, under far-field channel propagation conditions we define the array response at the RIS for the steering angles  $\bar{\theta}$ ,  $\bar{\phi}$  along the azimuth and elevation, respectively, as

$$\mathbf{a}(\bar{\theta}, \bar{\phi}) \triangleq \mathbf{a}_x(\bar{\theta}) \otimes \mathbf{a}_y(\bar{\phi}) \quad (1)$$

$$= [1, e^{j2\pi\delta \cos(\bar{\theta})}, \dots, e^{j2\pi\delta(N_x-1)\cos(\bar{\theta})}] \otimes [1, e^{j2\pi\delta \sin(\bar{\phi})}, \dots, e^{j2\pi\delta(N_y-1)\sin(\bar{\phi})}] \in \mathbb{C}^{N \times 1}, \quad (2)$$

where  $\delta$  is the ratio between the antenna spacing and the signal wavelength (usually  $\delta = 0.5$ ). Assuming line-of-sight signal propagation and a single-antenna transmitter, the channel between the latter and the RIS is given by

$$\mathbf{g} \triangleq \sqrt{\gamma_t} \mathbf{a}(\theta_t, \phi_t) \in \mathbb{C}^{N \times 1}, \quad (3)$$

where we define the average channel power gain as  $\gamma_t \triangleq \beta_0/d_t^2$ , with  $\beta_0$  the average channel power gain at a reference distance.  $d_t$  represents the distance between the transmitter and the RIS, whereas  $\theta_t$  and  $\phi_t$  denote the angles of arrival at the RIS along the azimuth and elevation, respectively. With similar reasoning, the channel between the RIS and the single-antenna receiver is given by

$$\mathbf{h} \triangleq \sqrt{\gamma_r} \mathbf{a}(\theta_r, \phi_r) \in \mathbb{C}^{N \times 1}. \quad (4)$$

The matrix containing the RIS configuration is defined as

$$\mathbf{\Phi} \triangleq \text{diag}[e^{j\psi_1}, \dots, e^{j\psi_N}] \in \mathbb{C}^{N \times N}, \quad (5)$$

with  $\psi_n \in \mathcal{Q}$ ,  $\forall n$  and  $\mathcal{Q}$  the quantized RIS phase shift set. Note that, to preserve a tractable model in (5), we have neglected any phase-dependent reflection coefficient at the RIS. Lastly, the received signal at the receiver is given by

$$y \triangleq \mathbf{h}^H \mathbf{\Phi} \mathbf{g} s + n \in \mathbb{C}, \quad (6)$$

where  $s \in \mathbb{C}$  is the transmitted symbol and  $n \in \mathbb{C}$  is the noise term distributed as  $\mathcal{CN}(0, \sigma_n^2)$ .

Let  $\mathbf{v} \triangleq \text{diag}(\mathbf{\Phi}^H) \in \mathbb{C}^{N \times 1}$  and  $\bar{\mathbf{h}} \triangleq \text{diag}(\mathbf{h}^H) \mathbf{g} \in \mathbb{C}^{N \times 1}$ , such that the power at the receiver is maximized by letting [19]

$$\mathbf{v} = \exp[j f_q(\angle \bar{\mathbf{h}})], \quad (7)$$

where  $f_q(\cdot)$  projects each element of the vector  $\angle \bar{\mathbf{h}}$  in (7) onto the closest element of set  $\mathcal{Q}$  to obtain a feasible solution.

It is important to highlight that vector  $\bar{\mathbf{h}}$  has the form of a scaling term times the UPA response vector in (1) for some

steering angles  $(\theta, \phi)$ . Hence, in order to design a codebook for RIS beamforming vectors, we artificially create  $N_B$  pairs of  $\{(\theta_n, \phi_n)\}_{n=1}^{N_B}$  couples and generate the corresponding UPA response vectors  $\{\mathbf{h}_n\}_{n=1}^{N_B}$ . Given the symmetry of the array response around the  $x$ -axis for the azimuth and around the  $y$ -axis for the elevation, and in the interest of saving measurement time, we sample a regular grid of points spaced by 3 degrees in the search space  $[-\frac{\pi}{2}, \frac{\pi}{2}] \times [-\frac{\pi}{4}, \frac{\pi}{4}]$ , such that  $N_B = 1891$ . Finally, we obtain the RIS configurations  $\mathcal{V} := \{\mathbf{v}_n\}_{n=1}^{N_B}$  for each steering angle couple  $\{(\theta_n, \phi_n)\}_{n=1}^{N_B}$  in the codebook by applying the expression in (7).

#### 4.2. Near-field codebook

The aforementioned channel model and associated codebook design are valid in the far-field of the RIS, i.e., beyond the threshold of  $2\frac{D^2}{\lambda}$ , where  $D$  is the maximum distance between any two elements in the RIS. However, in this paper, we perform experiments with multiple RIS boards forming a larger structure, by exploiting the modularity of our design. Hence, the likelihood of a user being in the near-field of the RIS is non-negligible. For example, compared to a single  $10 \times 10$  RIS board whose far-field threshold is 6.5 m, in the case of a  $10 \times 20$  RIS setup, i.e. two RIS boards connected horizontally, the far-field threshold is increased by 2.5 times. Whereas, in a  $20 \times 20$  RIS setup, i.e., four RIS boards connected to form a squared array, it is increased by 4 times. As a result, the wavefront of the RIS channel link exhibits a non-negligible curvature. To deal with this issue, we develop a near-field codebook in the following way. Let  $\mathbf{Q} = [\mathbf{q}_1, \dots, \mathbf{q}_N] \in \mathbb{R}^{3 \times N}$  denote the matrix containing the 3D positions of the RIS unit cells, while  $\mathbf{p}_{\text{TX}} \in \mathbb{R}^{3 \times N}$  and  $\mathbf{p}_{\text{RX}} \in \mathbb{R}^{3 \times N}$  denote the 3D position of the transmitter and receiver, respectively. Hence, we express the near-field channel coefficient between the transmitter and the  $p$ -th unit cell at the RIS as

$$g_p^{nf} = \sqrt{\frac{\beta_0}{\|\mathbf{q}_p - \mathbf{p}_{\text{TX}}\|^2}} e^{j\frac{2\pi}{\lambda}\|\mathbf{q}_p - \mathbf{p}_{\text{TX}}\|}, \quad p = 1, \dots, N \quad (8)$$

Similarly, the channel coefficient between the  $p$ -th unit cell at the RIS and the receiver is given by

$$h_p^{nf} = \sqrt{\frac{\beta_0}{\|\mathbf{q}_p - \mathbf{p}_{\text{RX}}\|^2}} e^{j\frac{2\pi}{\lambda}\|\mathbf{q}_p - \mathbf{p}_{\text{RX}}\|}, \quad p = 1, \dots, N. \quad (9)$$

In order to build a beamforming codebook, we fix the position of the transmitter and the associated value of channel  $\mathbf{g}^{nf}$  according to (8), while we vary the position of the receiver as

$$\mathbf{p}_{\text{RX}}(\theta_r, \phi_r) = d_r \begin{bmatrix} \cos(\theta_r) \sin(\phi_r) \\ \sin(\theta_r) \sin(\phi_r) \\ \cos(\phi_r) \end{bmatrix}. \quad (10)$$

We remark here that the choice of  $d_r$  is irrelevant to the design of the codebook, since the RIS is able to control only the phase of the impinging signal. Therefore, we fix the value of  $d_r$  and artificially create  $N_B$  pairs of  $\{(\theta_m, \phi_m)\}_{m=1}^{N_B}$  couples on a 3D sphere with given uniform spacing. Finally, as detailed in §4,

we obtain the RIS configurations  $\mathcal{V} := \{\mathbf{v}_n\}_{n=1}^{N_B}$  by constructing the equivalent channel  $\bar{\mathbf{h}}^{nf}(\theta_r, \phi_r) = \text{diag}(\mathbf{h}^{nf}(\theta_r, \phi_r)^H) \mathbf{g}^{nf} \in \mathbb{C}^{N \times 1}$  and the associated RIS configuration by applying (7) for every  $(\theta_m, \phi_m)$  couple.

#### 4.3. Multi-beam RIS configuration

In this section, we detail the proposed approach to design a multi-beam RIS configuration, i.e., a configuration in which the signal reflected at the RIS is maximized at multiple locations in space (e.g., for multicast communications). To this end, we employ the max-min framework described in [20].

Let  $\{\mathbf{h}_k\}_{k=1}^K$  denote the set of channels corresponding to the  $K$  users whose received signal should be maximized. The optimized multi-beam RIS configuration is obtained by solving the following problem

$$\begin{aligned} \max_{\mathbf{v}} \quad & \min_{k=1, \dots, K} \|\mathbf{v}^H \bar{\mathbf{h}}_k\|^2 \\ \text{s.t.} \quad & |v_p|^2 = 1, \quad p = 1, \dots, N \end{aligned} \quad (11)$$

where we have defined the equivalent channel to each user  $k$  as  $\bar{\mathbf{h}}_k = \text{diag}(\mathbf{h}_k^H) \mathbf{g}$ . Note that both  $\mathbf{g}$  and each  $\mathbf{h}_k$  can be constructed according to (3)-(4) or (8)-(9) depending on the associated distance between the transmitter and the RIS, and between the  $k$ -th user and the RIS, respectively.

Problem (11) is non-convex due to the constraint on each element of the RIS configuration vector  $\mathbf{v}$ , which is required to ensure that there is no signal amplification, and, moreover, since it implies the maximization of a convex objective function. To deal with this issue, we employ semidefinite relaxation as follows. Let  $\mathbf{V} = \mathbf{v}\mathbf{v}^H \in \mathbb{C}^{N \times N}$  and  $\bar{\mathbf{H}}_k = \bar{\mathbf{h}}_k \bar{\mathbf{h}}_k^H \in \mathbb{C}^{N \times N}$ , such that Problem (11) is rewritten as

$$\begin{aligned} \max_{\mathbf{V} \succeq 0} \quad & \min_{k=1, \dots, K} \text{tr}(\mathbf{V} \bar{\mathbf{H}}_k) \\ \text{s.t.} \quad & \text{diag}(\mathbf{V}) = \mathbf{1}, \quad \text{rank}(\mathbf{V}) = 1. \end{aligned} \quad (12)$$

Problem (12) is solved by ignoring the non-convex rank constraint and thus obtaining the optimized matrix  $\mathbf{V}^*$  with standard semidefinite programming, such as CVX. Finally, we extract the (rank-1) optimized RIS configuration  $\mathbf{v}$  by employing Gaussian randomization on  $\mathbf{V}^*$ .

### 5. Prototype Implementation

We prototyped our design using a two-layered PCB (Printed Circuit Board). The substrate material is FR-4, a composite material made of woven fiberglass with an epoxy resin binder that is flame resistant. Its relative electrical permittivity is in the range of  $\epsilon_r = [4.1, 4.8]$ , and is coated by two layers of 1-ounce copper ( $35 \mu\text{m}$ ). In general, thick substrates and high permittivity lead to small bandwidths and low efficiency due to surface waves [21]. Since the operating frequency of our prototype is  $f = 5.3 \text{ GHz}$  ( $\lambda = 56.56 \text{ mm}$ ), we chose a substrate thickness of  $h = 0.53 \text{ mm}$ , that is in the range  $0.003\lambda \leq h \leq 0.05\lambda$  as suggested in [21].



### 5.1. Patch Antenna

Patch antennas are implemented by cutting out a particular shape from the copper of the board's upper layer. In this way, the remaining metallic shape can radiate at the desired frequency while the back layer operates as ground for the antenna. Following the conventional literature on antenna design, we used a rectangular shape, as shown in Fig. 4. In more detail, we used the transmission-line model from [22] to calculate its width  $W$  and length  $L$  as follows:

$$W = \frac{\lambda}{2\sqrt{0.5(\epsilon_r + 1)}} = 16.9 \text{ mm}, \quad (13)$$

$$L = L_{eff} - 2\Delta L = 13.15 \text{ mm}, \quad (14)$$

where  $\epsilon_{eff} = \frac{\epsilon_r + 1}{2} + \frac{\epsilon_r - 1}{2} \left( \frac{1}{\sqrt{1 + 12 \frac{h}{w}}} \right)$  is the effective dielectric constant that takes into account the fact that the electric field lines reside in the substrate and partially in the air,  $L_{eff} = \frac{c}{2f\sqrt{\epsilon_{eff}}}$  is the effective length,  $c$  is the speed of light, and  $\Delta L = 0.412h \cdot \frac{\epsilon_{eff} + 0.3}{\epsilon_{eff} - 0.258} \cdot \frac{\frac{h}{w} + 0.264}{\frac{h}{w} + 0.8}$  is an offset to obtain the antenna physical length from  $L_{eff}$  (see [22] for details).

As shown in Fig. 4, a microstrip connects each antenna to the RF switch. To this end, we selected an *inset feeding* approach, with a notch at the edge of the antenna. This approach allows us to adapt the antenna to a precise characteristic impedance, which is crucial for maximizing power transfer. Given this notch (see details later), we refined the geometry derived before with the parameters shown in Fig. 4 by exhaustive search using a full-wave simulator [23], thus setting  $W = 15.5 \text{ mm}$  and  $L = 12.8 \text{ mm}$ .

In the following, we elaborate on two crucial parameters: (i) the width of the microstrip that connects the RF switch (see Fig. 1), and (ii) the position of the notch. The former is essential to guarantee impedance-matching, and, since the usual characteristic impedance is  $50 \Omega$ , the width of all the microstrips must be selected accordingly.

#### 5.1.1. Width of the feeding line

To avoid power loss between the feeding line and the RF switch, their characteristic impedance should match. Therefore, we used the model described in [24] to estimate a 0.95-mm line width, which equalizes the  $50 \Omega$ -impedance of the switch.

To validate this, we printed a 0.95mm-width microstrip and applied the Time Domain Reflectometry (TDR) technique using a Vector Network Analyzer (VNA) to measure the actual characteristic impedance along the line. TDR generates a pulse with

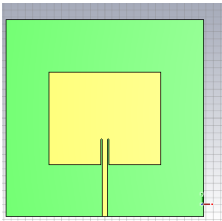


Figure 4: Layout of the patch antenna design.

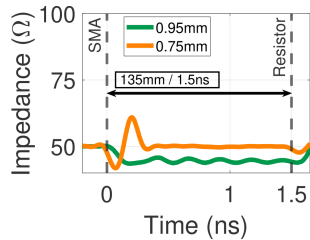


Figure 5: TDR chart of a 0.95mm-width microstrip.

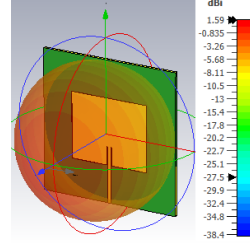


Figure 6: Expected reflection pattern of the patch antenna.

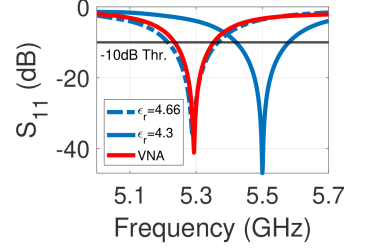


Figure 7:  $S_{11}$  parameter of two patch antenna samples.

a short rising time that allows us to calculate the impedance along the line based on the received reflections.

As depicted in Fig. 5 (green), this experiment shows that the actual impedance along the line is smaller than the predicted  $50 \Omega$ . Such a mismatch with the impedance of the switch would incur some power loss at every unit cell and, consequently, poor beamforming gains overall.

Consequently, we opted for a simple empirical approach: we printed out several 135mm-length microstrips with different widths, and applied the TDR method to each sample. Fig. 5 shows with an orange line the result of the selected sample, with a width equal to 0.75 mm, which provided the best performance. Ignoring the large oscillation at the beginning of the line, which is due to the soldered SMA connector that we used to connect the line and the VNA, the experiment shows a perfect match with the expected value of  $50 \Omega$ .

#### 5.1.2. Notch

The second relevant parameter is the depth of the notch, which should minimize the amount of reflected power. This is achieved when the impedance of the antenna matches that of the feeding line. However, the antenna's impedance diminishes as one moves towards its center because the current's intensity is higher at that point. Hence, it is important to carefully design the depth of the notch.

Following the analytical method introduced in [22], we first estimated the impedance at the bottom edge of the antenna and centered on the horizontal plane (see red bullet in Fig. 4). At this point, the impedance is purely resistive, i.e., its reactance is zero, and should be equal to  $R_{edge} \approx 341 \Omega$  (the details of the mathematical model can be found in [22]). Then, the optimal depth of the notch can be computed as:

$$h_{\text{notch}} = \frac{L}{\pi} \cos^{-1} \left( \sqrt{\frac{R}{R_{edge}}} \right) \approx 4.9 \text{ mm}, \quad (15)$$

where  $R$  is the desired impedance (i.e.,  $50 \Omega$ ).

We attempted to validate this result with the full-wave simulator [23] and found that a 3.5-mm depth, cutting across the patch antenna as shown in Fig. 4, maximizes performance ( $\sim 30\%$  difference with respect to the model). Fig. 7 shows with a blue line the amount of power that is reflected, estimated by the simulator and referred to as  $S_{11}$  parameter in antenna design. The result shows good performance at 5.5 GHz, the operating frequency of choice. Fig. 6 shows the simulated reflection pattern, with minimal backwards propagation. Note that the an-

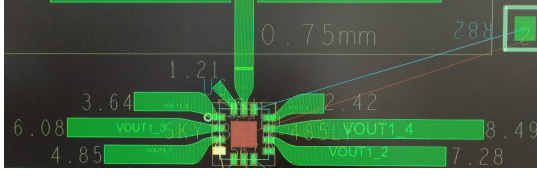


Figure 8: RF switch and microstrips.

Output port	7	6	5	1	3	2	4
$\varphi$ (deg)	51.42	102.85	154.28	205.71	257.14	308.57	360
$l$ (mm)	1.21	2.42	3.64	4.85	6.08	7.28	8.49

Table 1: RF switch's output ports, the length of the associated delay lines, and the resulting phase shifts.

tenna is not very directive and has an expected gain of 1.5dBi, which is common for this type of low-cost antennas.

To validate the patch design, we printed a sample antenna with the aforementioned parameters. Using our VNA, we measured the empirical  $S_{11}$  and plotted the result with a red line in Fig. 7. Perhaps surprisingly, the minimal- $S_{11}$  frequency point is 5.3 GHz instead of the intended 5.5 GHz. After some research, we realized that the offset stems from an error on the nominal permittivity  $\epsilon_r = 4.3$  used in our model/simulations for the PCB substrate. After some iterations with our simulator, we estimated the real permittivity to be  $\epsilon_r = 4.66$ . In light of this, we changed the operating frequency to  $f = 5.3$  GHz.

From Fig. 7, we can also estimate that the bandwidth of our approach, i.e., the range of frequencies where the antenna's  $S_{11}$  is  $\leq -10$  dB, is 118MHz (note the black horizontal line). We finally note that, at 5.3 GHz, the  $S_{11}$  is -41 dB, which corresponds to a Voltage Standing Wave Ration (VSWR) of 1.018. This means that the amount of power from the feeding line that is reflected back is negligible, which was our goal.

## 5.2. Phase shifters

At each cell, a specific phase shift  $\varphi$  is applied by *routing* the RF signal towards a specific delay line, implemented with a microstrip, that reflects the signal back to the patch antenna. To this end, we use a 3-bit RF switch SKY13418-485LF [25], which has 1 input port (attached to the feeding line), 3 configuration ports (more later), and 8 output ports connected to delay lines of different lengths. Given one configuration (input-output port mapping encoded as 3 bits in the configuration ports), the resulting phase shift follows as:

$$\varphi = \frac{360 \cdot 2l \cdot f}{c \cdot v_f}, \quad (16)$$

where  $l$  denotes the distance travelled from the patch antenna to the end of the delay line (including the switch and the feeding and delay lines), and  $v_f$  is the velocity factor of the microstrip material. Note that  $2l$  accounts for the round-trip between antenna and delay line.

To estimate  $v_f$  empirically, we take advantage of the TDR technique used earlier, which also measures the time  $d_{\text{microstrip}}$  it takes for a signal to travel through a microstrip of length  $l_{\text{microstrip}}$ . As shown in Fig. 5,  $d_{\text{microstrip}} = 1.51$  ns for a line of  $l_{\text{microstrip}} = 135$  mm, which is sufficiently long to force the signal to travel at

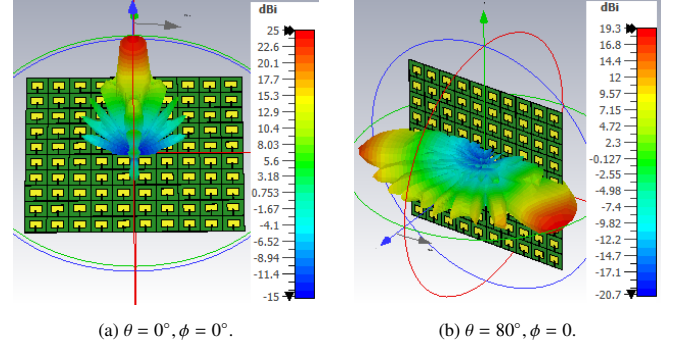


Figure 9: Expected beamforming pattern of a  $10 \times 10$  RIS.

least  $2\lambda$  and hence enable highly accurate delay estimates. We then calculate  $v_f = \frac{v_{\text{microstrip}}}{c} = 0.298 \approx 0.3$ , where  $v_{\text{microstrip}} = \frac{l_{\text{microstrip}}}{d_{\text{microstrip}}}$  is the velocity of the signal through the microstrip.

Given  $v_f$  and the selected microstrips width derived in §5.1.1 (0.75 mm), we can calculate the length of the delay lines corresponding to the phase shifts that need to be encoded into each output port, as indicated in Table 1. Note that port 8 has no associated phase shift. Instead, this port connects with a delay line that ends with a  $50\Omega$ -resistor, which prevents the signal to be reflected back. We refer to this configuration as “absorption state”, which enables us to build *virtual* RISs of any size and shape. Alternatively, an energy harvester [17] can be used to feed the MCU and effectively make it self-sustainable. The resulting design is shown in Fig. 8.

## 5.3. Microcontroller Unit (MCU)

As explained in §3, an MCU is in charge of parametrizing the configuration ports of the RF switch in each unit cell. We have selected the STM32L071V8T6 MCU from STMicroelectronics [26], which is low cost (see §7), high-speed (configuring 100 cells takes  $< 35$  ms), and low energy-consuming (62 mW in high-performing mode). We note that we have not optimized the MCU, which we leave for future work. For instance, we only use the MCU's high-performance (high-consuming) mode, although it provides low-consuming modes too. Exploiting these modes could reduce its energy consumption to the order of  $\mu\text{W}$ , which is amenable to energy harvesters [17].

## 5.4. RIS board

The spacing between unit cells (antennas) has to be carefully designed to maximize beamforming gains. Roughly speaking, a small spacing increases the probability of mutual coupling, which decreases the efficiency of each antenna because of surface waves propagation. Conversely, a large spacing leads to grating lobes, as we demonstrate in §6. All in all, the inter-cell spacing depends on the maximum steering angle  $\theta_{\text{max}}$  of the main lobe, which is given by  $d_{\text{max}} = \frac{\lambda}{1 + \sin(\theta_{\text{max}})}$ . Note that, though  $d_{\text{max}} = \lambda/2$  maximizes the steering angle range of the array,  $\theta_{\text{max}} = 90^\circ$  is not achievable in practice [27].

Prior to developing a prototype, we simulated a  $10 \times 10$  RIS board with a regular  $10 \times 10$  planar antenna array. In our first set of simulations, each antenna element is fed with equal power

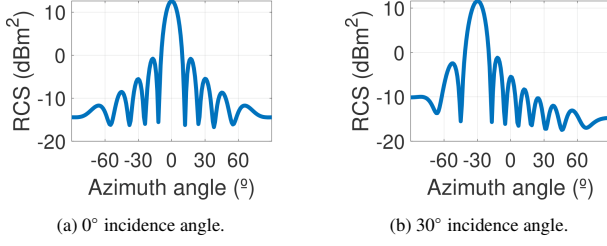


Figure 10: RCS of a  $10 \times 10$  RIS illuminated by a plane wave.

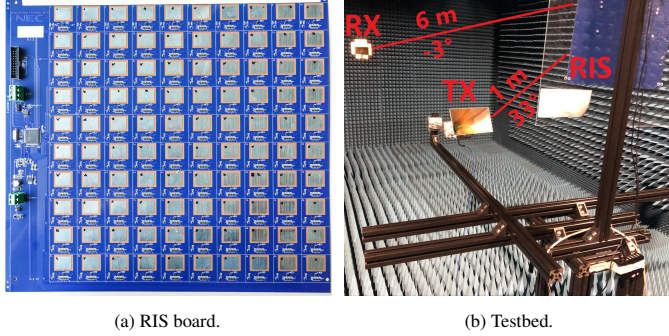


Figure 11: (a)  $10 \times 10$  RIS PCB realization, and (b) testbed in an anechoic chamber with rotating structure.

from an open-ended transmission line that induces a phase delay that is optimized offline to maximize power towards the selected azimuth and elevation angles. Figs. 9a and 9b show the expected reflection pattern of two different configurations that maximize power towards an elevation of  $\phi = 0^\circ$  and, respectively, an azimuth of  $\theta = \{0^\circ, 80^\circ\}$ .

On the one hand, we can observe from Fig. 9a that the array can achieve a narrow beam pattern, with a Half Power Beamwidth (HPBW) equal to  $10.1^\circ$ , with a gain of 25 dBi in the intended direction, which halves with a 10-degree offset. No back-radiation is expected. On the other hand, Fig. 9b shows that a large steering angle of  $\theta = 80^\circ$  dissipates half the energy towards the opposite direction and drops the power of the beam to 19.3 dBi.

Note however that the power radiated by a RIS comes from an external source that *illuminates* the surface. In order to simulate this behavior, we generated a plane wave linearly polarized, and measured the resulting Radar Cross Section (RCS). The RCS estimates how much of the incident power at every point of the surface is scattered back to the receiver. Hence, we expect high RCS values in the direction of the main beam and lower in other directions. This is indeed confirmed in Figs. 10a and 10b for an incidence angle of  $0^\circ$  and  $30^\circ$ , respectively. In both cases, the RIS is configured to reflect the received signal perpendicularly to the incidence angle of the received signal, i.e., the RIS should maximize power in the same direction of the incidence angle, which is confirmed by both figures with a RCS approximately equal to 12 – 13 dBsm in the intended direction. This highlights the fact that, in real life scenarios, the angle of arrival must be known to the controller to maximize beamforming gains.

We manufactured 10 boards of  $10 \times 10$  unit cells each. All

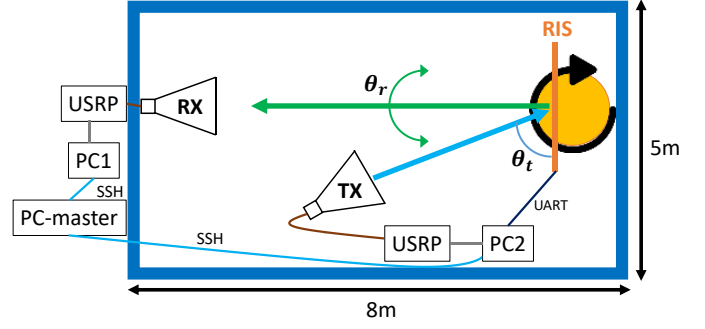


Figure 12: Map of the testbed.

the phase and selection buses, which connect each unit cell with an MCU, are built with microstrips. Unit cells are deployed in the PCB layout such that the same inter-cell distance can be maintained across co-located boards. The remaining elements described in §3 (flip-flops, resistors, etc.), are standard components assembled on the PCB. The final printout is shown in Fig. 11a.

## 6. Empirical Characterization

We characterized one of our  $10 \times 10$  RIS boards in an  $8 \text{ m} \times 5 \text{ m}$  anechoic chamber. Figs. 11b and 12 illustrate our testbed. We mounted the board on a turntable controlled remotely from a master PC, which is also used to configure the beamforming parameters of the RIS. We use two software-defined radio devices attached to horn antennas with gain  $G = 13.5$  dBi to generate (“TX”) and receive (“RX”) a continuous stream of OFDM QPSK-modulated symbols with 5 MHz of bandwidth and numerology that meets 3GPP LTE requirements. The transmission power of TX is -30 dBm per subcarrier, and we sample the reference signal received power (RSRP) at RX.

The distances RIS-TX and RIS-RX are  $d_{\text{RIS-TX}} = 1.1$  m and  $d_{\text{RIS-RX}} = 6.3$  m, respectively. Considering the size of the RIS and its operating frequency, it is hard to guarantee that  $d_{\text{RIS-TX}}$  is larger than the far-field threshold, which is  $2 \frac{D^2}{\lambda} = 6.5$  m [22] as detailed in §4.2. Nevertheless, our choice of  $d_{\text{RIS-TX}}$  is larger than the *reactive* near-field threshold, which is  $0.62 \sqrt{\frac{D^3}{\lambda}} = 0.73$  m [22], and sufficient for our purposes. As shown in Fig. 12, the rotation of the table determines the azimuth angle  $\theta_r$ , and the location of TX determines  $\theta_t$ . Conversely, the elevation angles of RIS-TX and RIS-RX are fixed to  $\phi_t = 33^\circ$  and  $\phi_r = -3^\circ$ , respectively.

### 6.1. Codebook characterization

We begin our experimental campaign by characterizing the codebook generated in §4.1. To this end, we test out all the configurations  $\mathcal{V} = \{\mathbf{v}_n\}_{n=1}^{N_B=1891}$  for a wide range of  $\theta_r = [-90^\circ, 90^\circ]$  and for  $\theta_t = \{20^\circ, 90^\circ\}$ .

For our empirical results, the first observation is that the direction  $(\theta_n, \phi_n)$  of the main lobe points towards  $(\theta_r - \theta_t, \phi_r - \phi_t)$ , as intended, for all configurations  $\mathbf{v}_n \in \mathcal{V}$ . These results, hence, validate our prototype for practically all configurations in  $\mathcal{V}$ . Figs. 13 and 14 depict some representative configurations  $\mathbf{v}_n \in \mathcal{V}$  for both  $\theta_t$  settings, respectively. These figures show that



the main beam points towards the intended directions. We note, however, that the gain of the main lobe is penalized when we use large steering angles (see, e.g.,  $\theta = 60^\circ$  in both figures), which is expected [27]. Overall, the power received in the intended direction ranges between  $-74$  dBm (for large steering angles) and  $-64$  dBm (for smaller angles), which give us remarkable beamforming gains between  $\sim 17$  dB and  $\sim 27$  dB over the noise floor.

Using the radar range equation in [22], the peak RCS can be calculated as  $64\pi^3 \frac{P_{RX}}{P_{TX}} \cdot \left( \frac{d_{RIS-TX} \cdot d_{RIS-RX}}{\lambda \cdot G} \right)^2 = 11.2 \text{ dBm}^2$ . Moreover, the HPBW is in average around  $10^\circ$  for all beampatterns. Both results are in line with our simulations in §5.4.

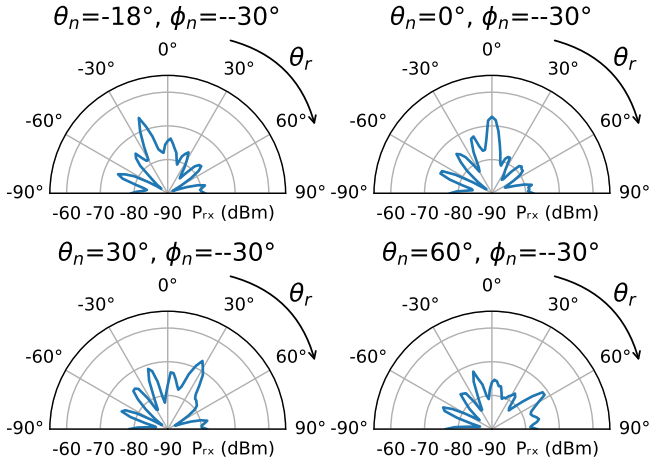


Figure 13: Examples of beampatterns for  $\theta_t = 90^\circ$ .

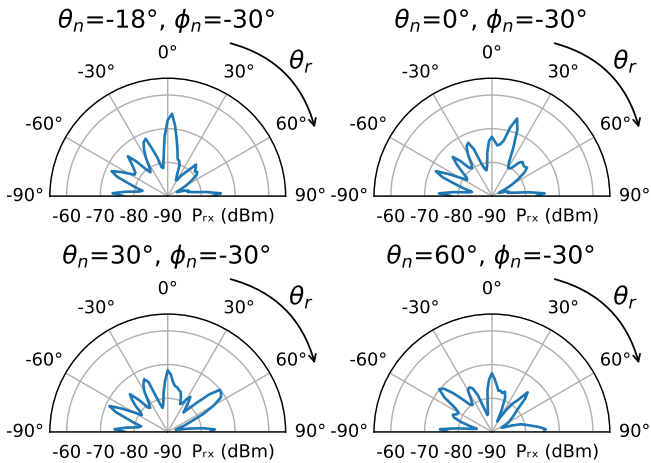


Figure 14: Examples of beampatterns for  $\theta_t = 20^\circ$ .

Next, we evaluate the ability to generate multi-beam patterns using the codebook described in §4.3. Specifically, we set two main beams at  $-10^\circ$  and  $30^\circ$ , respectively. Moreover, since we expect a necessary power drop at each of the two beams, we employ 2 RIS modules in a horizontal setup achieving an equivalent  $10 \times 20$  RIS. Fig. 15 confirms that a multi-beam pattern is achievable at the cost of sacrificing the maximum obtainable power, which is split into the two desired directions. The peaks of the two main beams are located at  $-9^\circ$  and at  $-35^\circ$ , with power

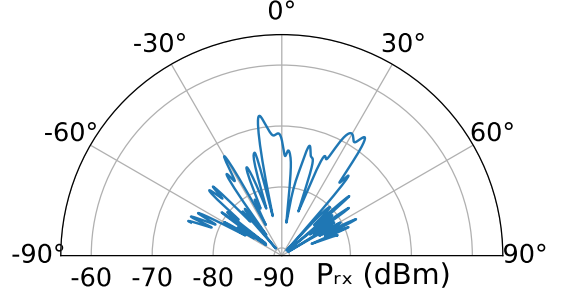


Figure 15: Reflection pattern of  $10 \times 20$  RIS setup (2 RIS boards) with multi-beam configuration.

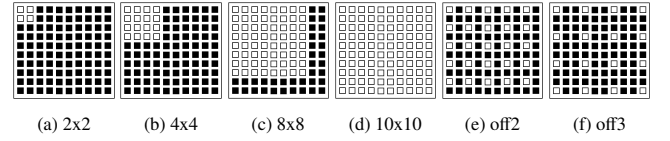


Figure 16: Different unit cell activation patterns in a  $10 \times 10$  RIS board. Colored squares represent deactivated (in black) and activated (in white) cells.

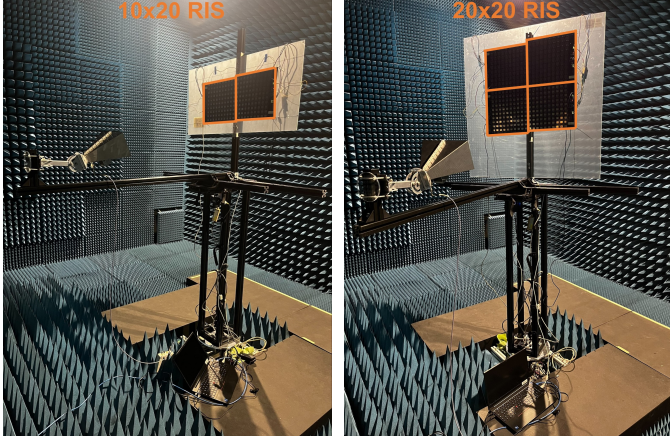
values of  $-66.5$  dBm and  $-66$  dBm, respectively. As expected, the multi-beam configuration results in a drop of 6 dBm with respect to the traditional single-beam case.

## 6.2. Scalability analysis

To assess scalability, we analyze the beamforming gain of our RIS for a variable number of unit cells. To this end, we first take advantage of the absorption state available at each unit cell of our RIS design in order to effectively reduce the number of antenna elements. Subsequently, we exploit the modularity feature of our RIS boards to easily scale up the number of antenna elements.

Thanks to the absorption state we can effectively create virtual RISs with different sizes and shapes by setting the activation patterns shown in Figs. 16a to 16d. For every virtual RIS, we re-optimized its codebook  $\mathcal{V}$  to account for its effective size and inter-element spacing. To ease the analysis, we now fix  $\theta_r = 0^\circ$  and  $\theta_t = 90^\circ$  and measure the power received for every configuration  $\mathbf{v} \in \mathcal{V}$ . The results are shown in Fig. 20, which represent the measured power with a color range for every combination of  $\theta$  (x-axis) and  $\phi$  (y-axis) from  $\mathcal{V}_N$ , and for  $N = \{4, 8, 64, 100\}$ . From these plots, we can observe how the main beam becomes sharper and carries more power as we increase  $N$ . With  $N = 4$  (top left plot), no configuration produces a distinguishable beam, which renders a  $2 \times 2$  virtual RIS ineffective. For the rest, we note a growing amount of power in the intended direction, respectively, equal to  $-81.8$  dBm ( $N = 16$ ),  $-71.5$  dBm ( $N = 64$ ), and  $-66.5$  dBm (all cells are activated). This behavior is expected: Fig. 22 depicts in red the power observed at RX with the optimal configuration  $\mathbf{v}$  as a function of  $N$ , and compares that with the mathematical model in [28] (see eq. (5) therein) represented in blue. Both results are remarkably close to each other, which validates the ability of our approach to effectively create virtual surfaces with different shapes.

As explained in §3, our RIS design is modular, enabling centralized control of multiple-appended RIS boards, which allows scaling up the reflective area of RIS structures seamlessly.



(a)  $10 \times 20$  RIS board setup with 2 horizontally-aligned RIS boards. (b)  $20 \times 20$  RIS board setup with 4 RIS boards forming a squared array.

Figure 17: Multi-board RIS tested in an anechoic chamber.

To empirically validate this, we mount together 2 RIS boards in a horizontal setup, which is equivalent to a  $10 \times 20$  RIS, with a total of 200 antenna elements, and 4 RIS boards in a squared setup, equivalent to a  $20 \times 20$  RIS with 400 antenna elements, as shown in Figs. 17a and 17b, respectively. All the distances and communication parameters are kept fixed as in the case of a single RIS board with  $\theta_t = 90^\circ$ .

As expected, having more antenna elements allows for reflecting more power in a narrower beam thanks to the beam-forming effect. The reflection pattern for the  $10x \times 20$  RIS case is depicted in Fig. 18. Here, the measured pattern exhibits a clear significant main beam at  $-3^\circ$ , with a reflected power peak of 60.5 dBm, HPBW of  $5^\circ$ , and sidelobes whose power is 10 dBm lower than the main beam. Compared to the single RIS board (with 100 antenna elements), the ratio between the peak power at the main beam and that at the sidelobes is significantly increased. Moreover, the measured peak power matches the aforementioned theoretical mathematical model trend as shown in Fig. 22.

In the  $20 \times 20$  RIS setup, we operate in an extreme near-field condition making measurements more challenging. Hence, we exploit the near-field codebook design detailed in §4.2 to deal with the non-negligible curvature of the wavefronts. The collected reflection pattern is shown in Fig. 19, where the main beam is located at  $-1^\circ$ , with a reflected power peak of 57 dBm. A difference of 10 dBm is maintained with the main sidelobes and the HPBW is again  $5^\circ$ . The increase in peak power is in line with the expected trend with a discrepancy of 3 dB compared with the mathematical model, mainly due to the extreme near-field condition.

Both multi-board RIS setups demonstrate that the modularity of our design allows us to conveniently scale up the number of elements at the RIS and obtain increasingly sharper and effective beamforming. Moreover, our measurements demonstrate that a near-field codebook design, tailored to the application scenario, is essential for successful RIS deployment.

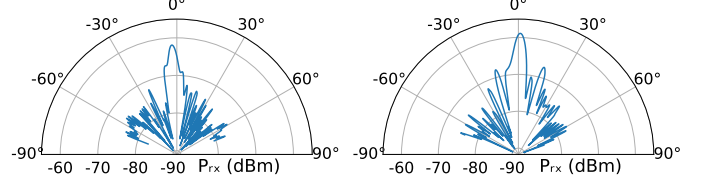


Figure 18: Reflection pattern of  $10 \times 20$  RIS (2 RIS coordinated boards).

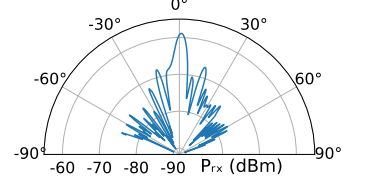


Figure 19: Reflection pattern of  $20 \times 20$  RIS (4 RIS coordinated boards).

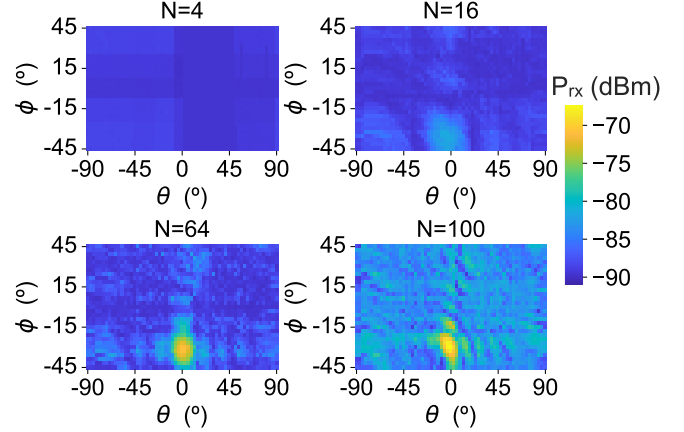


Figure 20: Received power over the respective optimal codebook  $\mathcal{V}_N$  for virtual RISs with different sizes (activation patterns of Figs. 16a-d, respectively).  $\theta_r = \theta_t = 0^\circ$ .

### 6.3. Other activation patterns

To conclude our characterization, we study the performance of our RIS prototype when the inter-cell distance differs from  $d_{max} = \lambda/2$  (shown in Fig. 20 for  $N = 100$ ). Like before, we calculated new optimized codebooks  $\mathcal{V}_{d_{max}}$  for  $d_{max} = \{\lambda, 1.5\lambda\}$ , and plot in Fig. 21 the power received at RX for each configuration  $\mathbf{v} \in \mathcal{V}_{d_{max}}$ . We do this for both activation patterns depicted in Fig. 16e (“off2”) and 16f (“off3”), for  $d_{max} = \lambda$  and  $d_{max} = 1.5\lambda$ , respectively.

By changing  $d_{max}$ , we also change the density of active cells per board,  $N = 25$  for  $d_{max} = \lambda$  (Fig. 21a) and  $N = 16$  for  $d_{max} = 1.5\lambda$  (Fig. 21b). As shown earlier, this has a cost in terms of beamforming gains that is also evidenced in Fig. 21: the maximum power is  $-80.4$  dBm and  $-84.2$  dBm for the two cases, respectively. Both plots reveal the presence of grating lobes, which are symmetrical beams that are denser for larger  $d_{max}$  values. These effects are well understood in the literature of antenna design and their distance can be estimated using

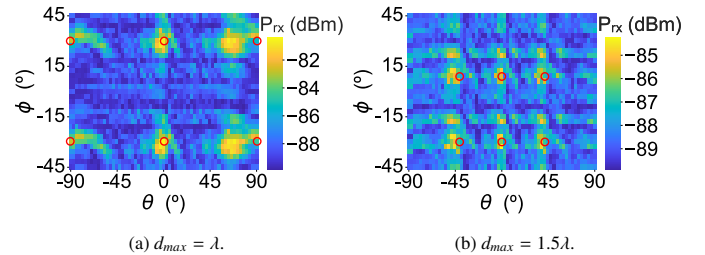


Figure 21: Received power over the respective optimal codebook  $\mathcal{V}_{d_{max}}$  for virtual RISs generating grating lobes (activation patterns of Figs. 16e-f, respectively). Red dots indicate the expected location of the lobes.  $\theta_r = \theta_t = 0^\circ$ .



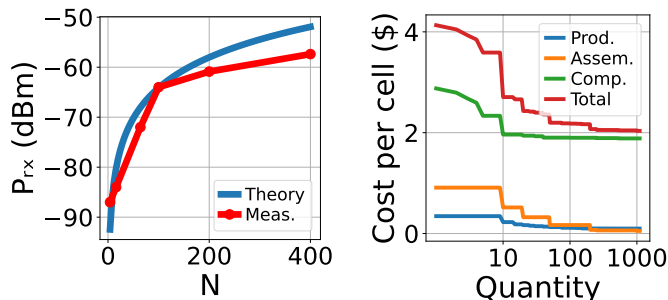


Figure 22: Beamforming gains as a function of the total number of antennas  $N$ .

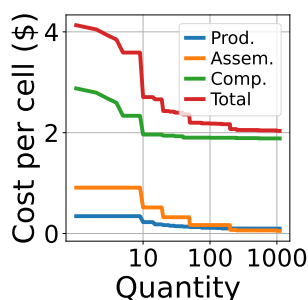
our model in §4. The figure depicts with red circles the expected location of these lobes, which match our measurements remarkably well. This further validates our design to effectively modify the shape of the RIS to the requirements of any given use case.

## 7. Reproducibility and future work

To conclude our paper, we provide some final remarks that shall help researchers in the RIS domain build on our results (dataset) and/or reproduce our RIS prototype and we discuss the future work to solve some limitations of design. Additionally, we discuss future work to address some design limitations.

For starters, we publicly release the dataset<sup>2</sup> we have generated during our empirical characterization in §6, which aggregates a total number of  $6.8 \cdot 10^6$  power samples. In the dataset, a RIS device is employed to sweep through the entire configuration codebook in every position of the turning table. Each row in the dataset corresponds to the main beam direction, expressed with a couple of angles  $(\theta_n, \phi_n)$ ; each column is associated with a different value of  $\theta_r$ , which indicates the rotation angle of the table. All power values in the cells are expressed in dBm. We strongly believe that this data can help other researchers study RIS-related problems without the need to build a prototype. For instance, this data can be exploited for the construction of a radiation pattern to be used in simulation or ray-tracing studies, which can ultimately lead to more realistic and accurate validation (see, e.g., [15]).

Next, we report the costs associated with building our prototype. For this purpose, we have used prices publicly available. There are three sources of cost to manufacture each board: (i) PCB production (including the patch antenna and the microstrips for the delay lines and the buses); (ii) additional electronic components (including RF switches, MCU, resistors, flip-flops, AND gates, etc.); and (iii) assembly all components onto the PCB. According to PCBWay [29], producing 10 PCB boards, as specified in our design, costs \$0.22 per unit cell; but it drops to \$0.11 and \$0.09 when the production scales up by 20x and 100x, respectively. Concerning additional electronic components, each 10x10 board bears 300 flip-flops, 100 AND gates,



100 RF switches, and 1 MCU. According to Digikey.de, the cost boils down to \$1.88 per unit cell when purchasing a batch of 1000 of such boards. The assembly process, according to PCBWay, scales down from \$0.51 to \$0.05 per cell when we scale up the number of boards from 10 to 1000 10x10-RISs. Fig. 23 depicts how these costs (normalized per unit cell) evolve with the manufacturing scale.

At the current stage, the RIS design has some limitations, which we consider for future work. The first one is related to the bandwidth of the antenna. Given that patch antennas are known to be narrowband, redesigning the RIS for a larger bandwidth may prove challenging, and alternative antenna types may need to be considered.

The second limitation involves the left-hand PCB area of each RIS board, which houses all the control components such as the MCU, serial connector, etc., as shown in Fig. 11a. This extra space prevents the placement of another board on the left side, as it would disrupt the inter-element distance of  $\lambda/2$ . In the next version of our RIS, this control area will be relocated to an external board that can be plugged into the back of the RIS, ensuring optimal placement of each RIS module.

The third limitation is the use of a resistor for the absorption mode, which dissipates all the incoming energy. A more efficient approach would be to store this unused power in a capacitor or battery to power the MCU and other components. Additionally, the MCU will be modified to enable deep sleep mode, conserving power when the RIS is idle. As per the datasheet, the power consumption in sleep mode can be significantly reduced to approximately  $1\mu W$ . This reduction could potentially enable the RIS to operate independently of the power grid through power harvesting. However, the development of a new protocol is necessary to effectively activate this state and awake the MCU after a predetermined time period or via an external interrupt.

## 8. Conclusion

In this paper, we underscored the transformative potential of Reconfigurable Intelligent Surfaces (RISs) for next-generation 6G networks. Our RF Switch-based RIS design achieves 3D beamforming passively, without the need for active RF components. Our design possesses two key innovations: a modular approach, which supports scalability, and high-resolution phase shifters, which enable fine-grained codebooks. Together, these elements coalesce into a multi-board passive RIS technology that champions sustainability for next-generation wireless systems. Moreover, we introduced strategies for multi-beam and near-field-capable codebooks emphasizing efficiency, precision, and reduced energy consumption. Our experiments in an anechoic chamber demonstrate the real-world scalability and practicality of our approach. By making our dataset publicly available, we aim to foster further innovations in the domain. As 6G looms on the horizon, our findings promote a sustainable and energy-efficient path forward in wireless technologies.

<sup>2</sup><https://github.com/marcantonio14/RIS-Power-Measurements-Dataset>

## Acknowledgments

The research leading to these results has been supported in part by SNS JU Project 6G-DISAC (GA no. 101139130) and ORIGAMI (no. 101139270).

## References

- [1] C. Pan, et al., Reconfigurable intelligent surfaces for 6g systems: Principles, applications, and research directions, *IEEE Communications Magazine* 59 (6) (2021) 14–20.
- [2] P. Mursia, S. Phang, V. Sciancalepore, G. Gradoni, M. D. Renzo, SARIS: Scattering aware reconfigurable intelligent surface model and optimization for complex propagation channels, *IEEE Wireless Communications Letters* (2023). doi:10.1109/LWC.2023.3299304.
- [3] M. Di Renzo, A. Zappone, M. Debbah, M.-S. Alouini, C. Yuen, J. de Rosny, S. Tretyakov, Smart radio environments empowered by reconfigurable intelligent surfaces: How it works, state of research, and the road ahead, *IEEE Journal on Selected Areas in Communications* 38 (11) (2020) 2450–2525. doi:10.1109/JSAC.2020.3007211.
- [4] A. Albanese, et al., MARISA: A Self-configuring Metasurfaces Absorption and Reflection Solution Towards 6G, in: *IEEE INFOCOM 2022 - IEEE Conference on Computer Communications*, 2022, pp. 250–259.
- [5] Z. Yang, et al., Energy-efficient wireless communications with distributed reconfigurable intelligent surfaces, *IEEE Transactions on Wireless Communications* 21 (1) (2022) 665–679.
- [6] M. Rossanese, P. Mursia, A. Garcia-Saavedra, V. Sciancalepore, A. Asadi, X. Costa-Perez, Designing, building, and characterizing rf switch-based reconfigurable intelligent surfaces, in: *Proceedings of the 16th ACM Workshop on Wireless Network Testbeds, Experimental evaluation & Characterization*, 2022, pp. 69–76.
- [7] L. Yezhen, et al., A novel 28 ghz phased array antenna for 5g mobile communications, *ZTE Communications* 18 (3) (2020) 20–25.
- [8] G. Trichopoulos, et al., Design and evaluation of reconfigurable intelligent surfaces in real-world environment, *arXiv preprint arXiv:2109.07763* (2021).
- [9] L. Dai, et al., Reconfigurable intelligent surface-based wireless communications: Antenna design, prototyping, and experimental results, *IEEE Access* 8 (2020) 45913–45923.
- [10] J. Hu, et al., Reconfigurable intelligent surface based rf sensing: Design, optimization, and implementation, *IEEE Journal on Selected Areas in Communications* 38 (11) (2020) 2700–2716.
- [11] R. Fara, et al., A prototype of reconfigurable intelligent surface with continuous control of the reflection phase, *arXiv preprint arXiv:2105.11862* (2021).
- [12] X. Tan, Z. Sun, D. Koutsonikolas, J. M. Jornet, Enabling indoor mobile millimeter-wave networks based on smart reflect-arrays, in: *IEEE INFOCOM 2018-IEEE Conference on Computer Communications*, IEEE, 2018, pp. 270–278.
- [13] V. Arun, H. Balakrishnan, Rfocus: Beamforming using thousands of passive antennas, in: *USENIX NSDI*, 2020, pp. 1047–1061.
- [14] M. Dunna, et al., Scattermimo: Enabling virtual mimo with smart surfaces, in: *ACM MobiCom*, 2020, pp. 1–14.
- [15] M. Rossanese, A. Garcia-Saavedra, A. E. Lutu, X. Costa Perez, Data-driven analysis of the cost-performance trade-off of reconfigurable intelligent surfaces in a production network, *Proceedings of the ACM on Networking* 1 (CoNEXT3) (2023) 1–20.
- [16] P. Mursia, et al., RISMA: Reconfigurable Intelligent Surfaces Enabling Beamforming for IoT Massive Access, *IEEE Journal on Selected Areas in Communications* 39 (4) (2021) 1072–1085.
- [17] M. S. Mir, et al., PassiveLiFi: rethinking lifi for low-power and long range rf backscatter, in: *ACM MobiCom*, 2021, pp. 697–709.
- [18] E. Basar, et al., Wireless communications through reconfigurable intelligent surfaces, *IEEE access* 7 (2019) 116753–116773.
- [19] Q. Wu, et al., Intelligent Reflecting Surface Enhanced Wireless Network: Joint Active and Passive Beamforming Design, *IEEE Transactions on Wireless Communications* 18 (11) (2018) 5394–5409.
- [20] P. Mursia, F. Devoti, V. Sciancalepore, X. Costa-Pérez, Rise of flight: RIS-empowered uav communications for robust and reliable air-to-ground networks, *IEEE Open Journal of the Communications Society* 2 (2021) 1616–1629. doi:10.1109/OJCOMS.2021.3092604.
- [21] A. Pandey, *Practical microstrip and printed antenna design*, Artech House, 2019.
- [22] C. A. Balanis, *Antenna theory: analysis and design*, John Wiley & sons, 2016.
- [23] Dassault Systèmes, CST Studio Suite: Electromagnetic field simulation software, <https://www.3ds.com/products-services/simulia/products/cst-studio-suite/>, accessed: 2022-03-01 (2022).
- [24] Analog Devices, Microstrip and Stripline Design: MT-094 tutorial, <https://www.analog.com/media/en/training-seminars/tutorials/MT-094.pdf>, accessed: 2022-03-01 (2009).
- [25] Skyworks Solutions, Inc, SKY13418-485LF: 0.1 to 6.0 GHz SP8T Antenna Switch, [https://www.skyworksinc.com/-/media/SkyWorks/Documents/Products/701-800/SKY13418\\_485LF\\_201712F.pdf](https://www.skyworksinc.com/-/media/SkyWorks/Documents/Products/701-800/SKY13418_485LF_201712F.pdf), accessed: 2022-03-01 (2019).
- [26] STMicroelectronics, STM32L071V8: Ultra-low-power Arm Cortex-M0+ MCU with 64-Kbytes of Flash memory, 32 MHz CPU, <https://www.st.com/en/microcontrollers-microprocessors/stm32l071v8.html>, accessed: 2022-03-01 (2021).
- [27] P. Delos, B. Broughton, J. Kraft, Phased array antenna patterns—part 2: Grating lobes and beam squint, *26 Phased Array Antenna Patterns—Series* (2020) 39.
- [28] W. Tang, et al., Wireless communications with reconfigurable intelligent surface: Path loss modeling and experimental measurement, *IEEE Transactions on Wireless Communications* 20 (1) (2021) 421–439. doi:10.1109/TWC.2020.3024887.
- [29] PCBWay, PCB prototype and fabrication, <https://www.pcbway.com>.

## Biographies



**Marco Rossanese** received the B.Sc. and M.Sc. degrees in Telecommunication Engineering from Università degli Studi di Padova in 2017 and 2019, respectively. He is an Early Stage Researcher in the European project B5G MINTS H2020 MSCA-ITN. He is employed as a researcher at NEC Laboratories Europe GmbH in the 6G Networks team and he is enrolled as a Ph.D. student at the

Technische Universität of Darmstadt. He focuses his work on Reconfigurable Intelligent Surfaces (RIS).



**Placido Mursia** received the B.Sc. and M.Sc. (with honors) degrees in Telecommunication Engineering from Politecnico of Turin in 2015 and 2018, respectively. He obtained his Ph.D from Sorbonne Université of Paris, at the Communication Systems department of EURECOM in 2021. He is currently a research scientist in the 6GN group at NEC Laboratories Europe.

His research interests lie in convex optimization, signal processing and wireless communication.



**Andres Garcia-Saavedra** received his PhD degree from the University Carlos III of Madrid (UC3M) in 2013. He then joined Trinity College Dublin (TCD), Ireland, as a research fellow until 2015. Currently, he is a Principal Researcher at NEC Laboratories Europe. His research interests lie in the application of fundamental mathematics to real-life wireless communication systems.



**Vincenzo Sciancalepore** received his M.Sc. degree in Telecommunications Engineering and Telematics Engineering in 2011 and 2012, respectively, whereas in 2015, he received a double Ph.D. degree. Currently, he is a Principal Researcher at NEC Laboratories Europe, focusing his activity on reconfigurable intelligent surfaces. He is an Editor of the IEEE Transactions on Wireless Communications.



**Arash Asadi** is a research group leader at TU Darmstadt, leading the Wireless Communication and Sensing Lab (WISE). His research is focused on wireless communication and sensing for Beyond-5G/6G networks. He is a recipient of several awards, including Athena Young Investigator award from TU Darmstadt and outstanding PhD and master thesis awards from UC3M. Some of his papers on D2D communication have appeared in IEEE COMSOC best reading topics on D2D communication and IEEE COMSOC Tech Focus.



**Xavier Costa-Perez** is Scientific Director at i2Cat and Head of 5G/6G R&D at NEC Laboratories Europe, and a Research Professor at ICREA. His team generates research results which are regularly published at top scientific venues, produces innovations which have received several awards for successful technology transfers, participates in major European Commission R&D collaborative projects and contributes to standardization bodies. He received both his M.Sc. and Ph.D. degrees in Telecommunications from the Polytechnic University of Catalonia (UPC).